Coordination and Diffusion in Glyoxal-Based Electrolytes for Potassium-Ion Batteries

(article starts on next page)

Coordination and Diffusion in Glyoxal-Based Electrolytes for Potassium-Ion Batteries

Lea C. Meyer,[a, b] Patrik Johansson,[b, c] and Andrea Balducci*[a, b]

Glyoxal-based electrolytes have been identified as promising for potassium-ion batteries (PIBs). Here we investigate the properties of electrolytes containing potassium bis(fluorosulfonyl)imide (KFSI) in 1,1,2,2-tetra-ethoxy-ethane (tetra-ethyl-glyoxal, TEG) using density functional theory (DFT) calculations, Raman spectroscopy, and impedance spectroscopy. The coordination and configuration of the complexes possible to arise from coordination of the K^+ ions by FSI and TEG were investigated both from an energetic point of view as well as qualitatively determined via comparing experimental and artificial Raman spectra. Overall, the K^+ coordination depends heavily on the electrolyte composition with contributions both from FSI and TEG. Energetically the coordination by both the *trans* FSI anion conformer and the TEG solvent with four z-chain conformation is preferrable. From the spectroscopy we find that at lower concentrations, the predominant coordination is by TEG, whereas at higher concentrations, K^+ is coordinated mostly by FSI. Concerning the diffusion of ions, investigated by impedance spectroscopy, show that the diffusion of the potassium salt is faster as compared to lithium and sodium salts in comparable electrolytes.

Introduction

Today lithium-ion batteries (LIBs) are the energy storage system of choice for portable devices, electric vehicles and stationary storage.[1] However, due to the limited availability of lithium and price increases, research efforts have been directed towards alternative battery technologies, such as potassium-ion batteries (PIBs).[2]

The ionic radius of K^+ is larger as compared to Li^+, resulting in lower charge density and consequently weaker interactions with the electrolyte solvent molecules. As a consequence, solvated K^+ ions exhibit smaller Stokes radii as compared to solvated Li^+ ions, enabling faster ion transport.[3] A fast ion transport in the electrolyte is crucial for the power performance of batteries.[3a] Nevertheless, the larger ionic size of K^+ can result in a faster degradation of the active materials of the electrodes, which leads to a reduction in cyclability and capacity.[2c] Dhir et al.[3a] investigated the diffusion coefficient of

1.0 M potassium bis(fluorosulfonyl)imide (KFSI) in 1,2-dimethoxyethane (DME) using the steady-state galvanostatic restricted diffusion method. The diffusion coefficient was determined to be $D_{KFSI\,in\,DME} = 7.6 \cdot 10^{-10}\ m^2\,s^{-1}$ indicating that the diffusion in potassium-based organic electrolytes is slightly faster than that of equivalent electrolytes based on lithium and sodium salts.[3a] Li^+, Na^+ and K^+ also differ in terms of their desolvation energies. Utilizing density functional theory (DFT) calculations, Okoshi et al. showed that K^+ exhibits the lowest desolvation energy, which underlies the observed faster diffusion.[3b] Another approach for determining the diffusion coefficient is impedance spectroscopy. The Warburg impedance, which can only be quantified at low frequencies (< 0.5 Hz), is of particular significance for the determination of the diffusion coefficient.[4] To prevent an overlay of the diffusion in the electrolyte by contributions from diffusion within an intercalation electrode material in the impedance spectrum, it is necessary to use a non-intercalating material, such as potassium metal electrodes.[5] In summary, the larger ionic size of K^+ ensue faster diffusion in the electrolyte, but also causes faster degradation of the active materials of the electrodes, which leads to a reduction in cyclability and capacity.[2c]

In the last few years, several cathode and anode active materials for PIBs have been investigated.[2d] On the electrolyte side, some of us proposed glyoxal-based solvents, such as 1,1,2,2-tetra-ethoxy-ethane (tetra-ethyl-glyoxal, TEG), for PIBs and other energy storage devices, such as LIBs, electrical double layer capacitors (EDLC) and sodium-ion batteries (SIB).[6] TEG is an acetal of the aldehyde glyoxal and is structurally similar to the, for LIBs commonly used, diethyl carbonate (DEC). Many physicochemical properties, including viscosity and permittivity, of TEG and DEC are comparable, but TEG has the benefits of higher flash and boiling points.[6c,7]

In any metal-ion batteries, the electrolyte solvent is of fundamental importance, as the ion solvation significantly

[a] L. C. Meyer, A. Balducci
Institute for Technical Chemistry and Environmental Chemistry (ITUC) and Center for Energy and Environmental Chemistry Jena (CEEC Jena), Friedrich Schiller University Jena, Philosophenweg 7a, 07743 Jena, Germany
E-mail: andrea.balducci@uni-jena.de

[b] L. C. Meyer, P. Johansson, A. Balducci
Alistore-ERI European Research Institute, FR CNRS 3104, Hub de l'Energie, 15 Rue Baudelocque, 80039 Amiens, France

[c] P. Johansson
Department of Physics, Chalmers University of Technology, 41296 Gothenburg, Sweden

ChemPhysChem

Research Article
doi.org/10.1002/cphc.202400606

**Chemistry
Europe**
European Chemical
Societies Publishing

impacts both the formation of the solid electrolyte interphase (SEI) and influences the ion transport.[8] Therefore proper and detailed understanding of the ion-ion and ion-solvent inter-actions is crucial. For K^+ coordination, most often only the first solvation shell is considered, and furthermore only cation-solvent interactions.[3b,9] This is justified by the weak cation-anion interactions, when e.g. anions such as FSI or hexafluor-ophosphate (PF_6^-) are used.[3b,8b,9] However, this is far from generally applicable as it depends on the salt(s) and solvent(s) as well as the salt concentration. In the special case of highly concentrated electrolytes (HCEs), such as 5 M KFSI in DME, or weakly solvating electrolytes (WSEs), such as 1 M KFSI in 1,2-diethoxyethane (DEE), the first solvation shell contains not only solvent molecules but also anions of the potassium salt. This results in an anion-derived SEI layer and an improved electro-chemical performance of the PIBs.[8a] In general, a wide electro-chemical stability window (ESW) is necessary for battery usage, which is proportional to the gap between the LUMO and HOMO levels of all electrolyte components.[10] Characteristically, the solvents of WSEs exhibit very low permittivity, with dielectric constants ε most often < 5, which also applies to TEG (ε $= 2.55$). Therefore, for proper understanding of TEG-based electrolytes both K^+-TEG and K^+-FSI interactions must be considered.[6c,8a,11] In the coordination of K^+ by small solvent molecules, such as EC, it was found that between six to ten oxygen atoms coordination is possible for K^+, which represents an increased coordination number (CN) as compared to Li^+ and Na^+.[9]

Results and Discussion

First, the molecular structures of the solvent TEG and the anion FSI were optimized using DFT calculations, followed by an investigation of coordination possibilities for K^+ cations.

Subsequently, artificial Raman spectra were compared with experimentally obtained Raman spectra to elucidate the coordination of K^+ by FSI and TEG, as function of the electrolyte salt concentration. Finally, the diffusion of KFSI species in the TEG was determined by impedance spectroscopy.

FSI and TEG Conformations

For proper understanding of the speciation, the conformational equilibrium must first be established. Therefore, starting with the FSI anion (Figure 1a) the energetically most favourable conformers were studied. The most favourable is the *trans* FSI conformer, in which the fluorine atoms, exhibiting higher electronegativity than the oxygen atoms, are positioned on opposite sides, and thus minimizes repulsion. The second most stable conformer is *cis* FSI: $+4.2$ kJ/mol. The preference of these two conformers has also been validated for several electrolytes – both experimentally and computationally.[12]

Subsequently, a set of conformers of TEG was geometry optimized (Figure 1b). TEG has four side chains, consisting of O—CH_2—CH_3, which can be arranged either in *c* (c-chain) or *z* (z-chain) conformations. Due to steric hindrances and interactions between the atoms, the z-chain conformation is in general the energetically favoured. Therefore, the conformer with four z-chains (TEG_{4z}) exhibits the lowest energy among the four conformers geometry optimized and evaluated. For each c-chain replacing a z-chain, the energy increases by 3–5 kJ/mol, making TEG_{4c} the energetically least favourable conformer.

In the literature, most often only the most stable conformer is considered. However, since conformers within 20 kJ/mol for sure in principle can co-exist at room temperature, kT is *ca.* 2 kJ/mol, we need another way to ascertain the different conformers present. Therefore, artificial Raman spectra of the TEG conformers were compared with the experimentally
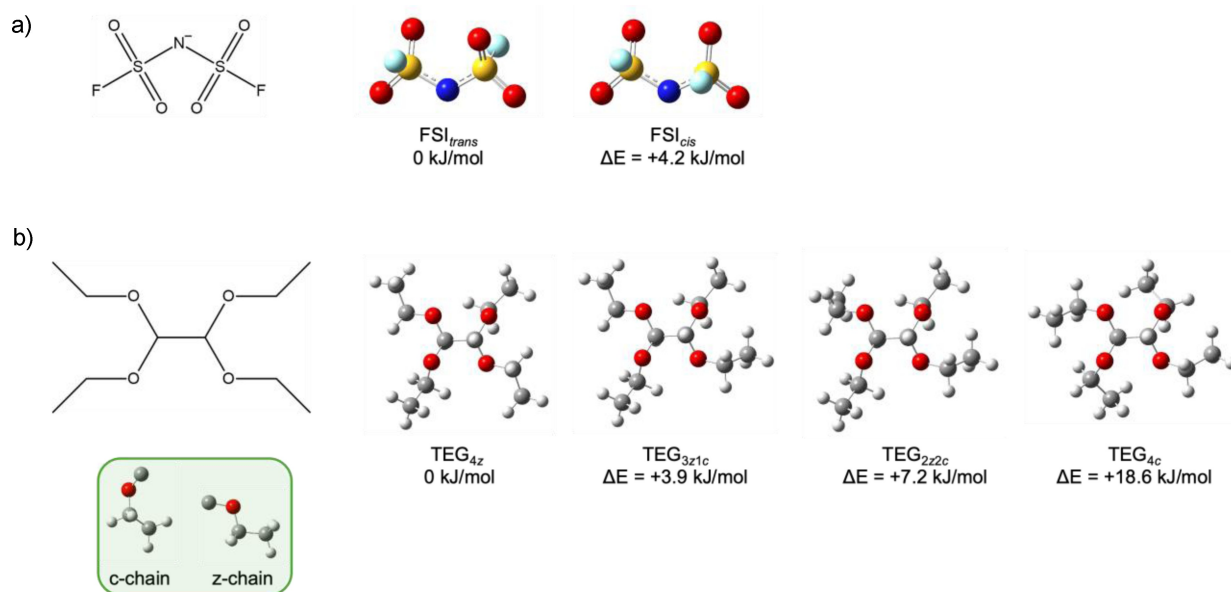

Figure 1. Structure, optimized geometries, and energies of a) FSI and b) TEG conformers.

ChemPhysChem

Research Article
doi.org/10.1002/cphc.202400606

Chemistry
Europe
European Chemical
Societies Publishing

measured Raman spectrum of TEG (Figure 2). In general, the former exhibits a red shift to lower wavenumbers by 30–35 cm^{-1}. Indeed, while the PCM model applied approximates a dielectric medium, it is more semi-quantitative. In the range 1200–1550 cm^{-1}, chosen due to few interfering bands and being where the bending modes of the CH$_2$ and CH$_3$ groups are located, the experimental peak at 1275 cm^{-1} thus can be matched with the computed peaks of both TEG$_{4z}$ and TEG$_{3z1c}$ at 1244 cm^{-1}. In contrast, TEG$_{2z2c}$ exhibits a doublet peak, and TEG$_{4z}$ shows a peak at significantly higher wavenumbers. On the other hand, the peak observed at 1450 cm^{-1} can best be explained by the broad features centred at ca. 1410 cm^{-1} from TEG$_{4z}$, TEG$_{3z1c}$, and/or TEG$_{2z2c}$. Given the left shoulder observed in the experimental spectrum and this only being present for TEG$_{2z2c}$, this conformer must also be present.

Overall, based on the energy differences and the comparison of artificial and experimental Raman spectra, there is a high probability that both TEG$_{4z}$ and TEG$_{3z1c}$ conformers are present in bulk TEG, as well as a small contribution of the TEG$_{2z2c}$ conformer, but no TEG$_{4z}$ conformer contribution.
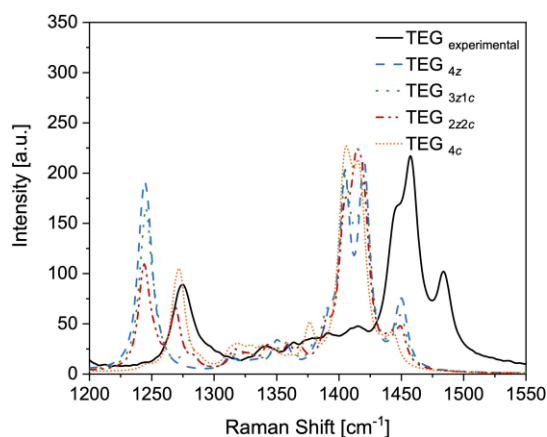

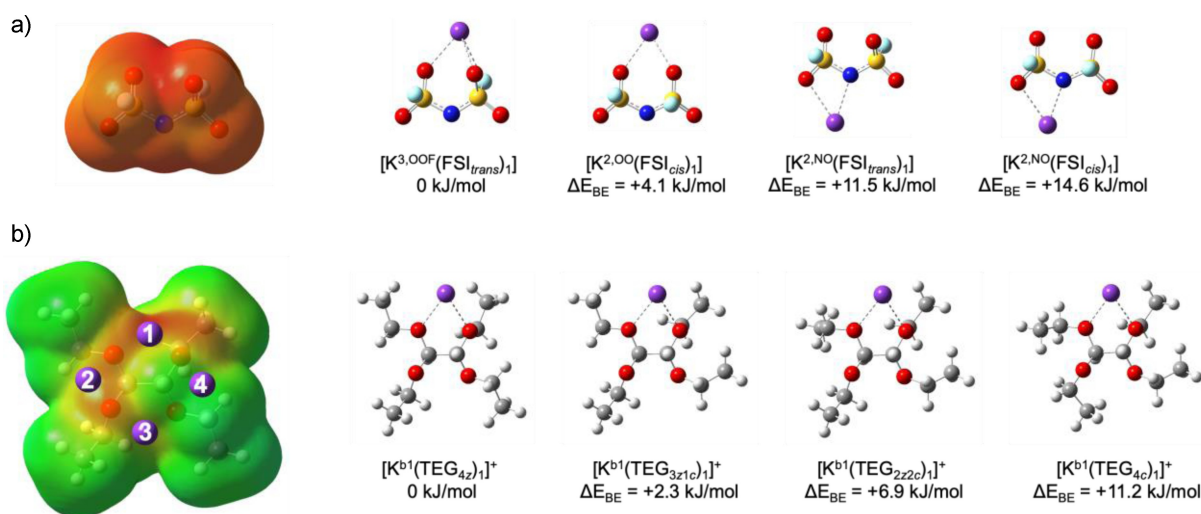**Figure 2.** Artificial and experimental Raman spectra of pure bulk TEG.

K$^+$ Coordination

Due to the low permittivity of TEG, both FSI and TEG coordination is likely to occur, and furthermore the chelating nature of TEG as ligand must be accounted for, as made for [K-DME]$^+$ complexes.[8b] Consequently, the solvation number (SN) can be lower than the CN.

Since K$^+$ is positively charged, they preferentially coordinate to negatively charged regions, depicted in red on the electrostatic potential (ESP) maps (Figure 3). While there exists no negatively charged region on the FSI, due to the single negative charge being delocalized over the whole anion, TEG exhibits regions of higher electronegativity between the oxygen atoms, providing generally four coordination possibilities for K$^+$ to TEG. Positions 1 and 3, located between O–C$_2$–O, are referred to as bridge coordination (K^{b1} and K^{b3}), and positions 2 and 4, located between O–C–O, as end-on coordination (K^{e2} and K^{e4}).

The two FSI conformers are either bidentately (K^2) or tridentately (K^3) coordinating K$^+$. The latter is only possible for *trans* FSI and is the energetically most favourable coordination. Overall, tridentate oxygen and fluorine atom coordination is preferred, followed by dual oxygen atom coordination, and then coordination to one nitrogen and one oxygen atom (Figure 3a).

For TEG, coordination at position 1 is preferred, followed by position 2, 3 and lastly (Figure S1). However, the energetically favourable configurations, which take both conformation and coordination into account, are those in which K$^+$ coordinates to TEG at position 1 in a bridge coordination (Figure 3b).

Comparing the binding energies for the [K-TEG$_1$]$^+$ and [K-FSI$_1$] complexes reveals that FSI forms a much stronger coordination with K$^+$ (Figure 4) and hence is likely to be present in the first cation solvation shell. Consequently, for complexes with SN > 1, a FSI ligand has to be in the first solvation shell and supplemented with additional TEG ligands. This results in the complexes [FSI$_1$-K-TEG$_1$] (SN = 2, CN = 5) and [FSI$_1$-K-TEG$_2$] (SN = 3, CN = 7). A complex with a higher SN number is not feasible due to the steric hindrance of the TEG molecule. The energeti-

Figure 3. ESP maps of the ligands, optimized geometries, and energies of a) [K-FSI$_1$] and b) [K-TEG$_1$]$^+$ configurations.

ChemPhysChem

Research Article
doi.org/10.1002/cphc.202400606

Chemistry Europe
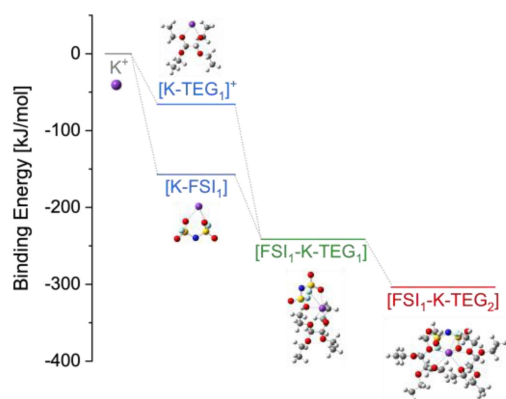European Chemical
Societies Publishing

Figure 4. Binding energies of solvated K$^+$ ions with FSI and TEG as ligands.

cally preferred configurations are those in which *trans* FSI coordinates tridentate and TEG coordinates to K$^+$ via the bridge 1 position. The bond length between K$^+$ and the donor atoms of the ligands increases by only 0.1 Å for complexes with SN $\geq$ 2, resulting in a bond length range of 2.7–2.9 Å. This bond length is comparable to that of K$^+$-O$_{DME}$ of 2.7 Å and longer than a Li$^+$—O$_{DME}$ bond of 1.9 Å.[11b] A longer distance, as

observed in the potassium ion coordination, here indicates a weaker bond, which in turn allows faster diffusion of K$^+$ as compared to Li$^+$ in the electrolyte.

Moving to electrochemical stability, the ESWs, molecules or complexes with lower lowest unoccupied molecular orbital (LUMO) levels are in general preferentially reduced at the anode.[13] The calculated K$^+$-complexes all exhibit lower LUMO energies than the pure TEG solvent (Figure 5) and hence reduced first. Vice versa, on the cathode side compounds with the higher highest occupied molecular orbital (HOMO) level are oxidized first.[10] For the glyoxal-based electrolytes, this would correspond to the prior decomposition of the pure solvent TEG. Combined and assuming that in a KFSI in TEG electrolyte, pure TEG as well as [FSI$_1$-K-TEG$_1$] and [FSI$_1$-K-TEG$_2$] complexes are present, an ESW of −1.6 eV (LUMO) to −8.9 eV (HOMO) can be achieved. The LUMO is lower that from DFT calculations for KFSI in DME and EC/DEC electrolytes made by Wang et al.[14]; −0.8 eV for DME and −0.9 eV for EC/DEC electrolytes, respectively, while for the HOMO −7.8 eV and −8.2 eV, respectively, were obtained. Thus, by using TEG as solvent, a lower HOMO was achieved, thereby the stability at the cathode enhanced and the oxidation of the electrolyte delayed until higher cell voltages.

Raman Spectroscopy

By analysing specific regions, it is possible to make statements about the existence of "free" FSI and TEG or K$^+$- complexes, depending on the concentration of the electrolyte. The region 660–760 cm^{-1} contains characteristic vibrations of "free" and coordinated FSI, while the region 800–950 cm^{-1} is characteristic for "free" and coordinated TEG (Figure 6).

In the FSI region, the single peak shifts very little, from 732 to 735 cm^{-1}, and the intensity increases, as the salt concentration increases. The corresponding vibration mode is a combination of S–F bond stretching ($\nu_{S\text{-}F}$) and S–N–S bending ($\delta_{S\text{-}N\text{-}S}$). The artificial Raman spectra show "free" FSI at 676 cm^{-1}, which is notably far from any experimental peak. However, it exhibits a red-shift upon cation coordination – most in the [K-FSI$_1$] model, with a too low and less realistic CN, less in the
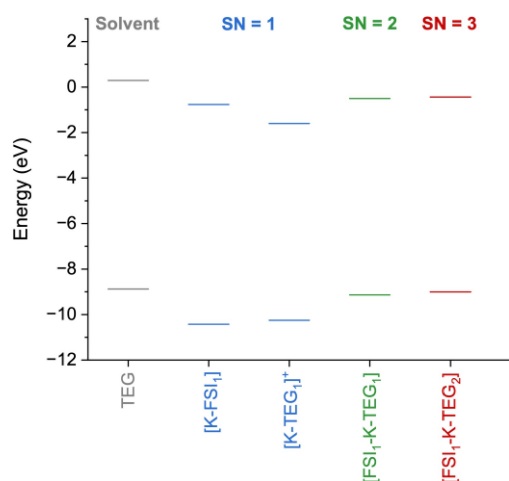

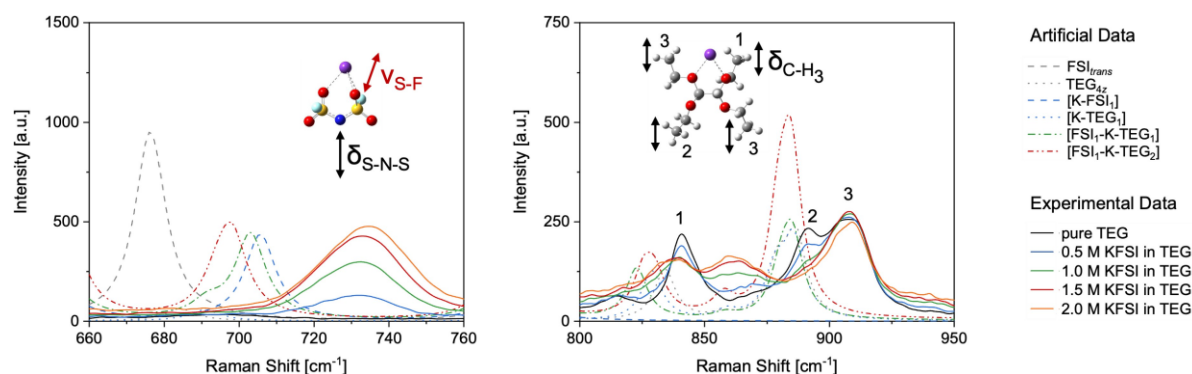**Figure 5.** Molecular energy levels of HOMO and LUMO for ligands and K$^+$ complexes.

Figure 6. Artificial and experimental Raman spectra of "free" FSI, "free" TEG and K$^+$ complexes (interrupted lines) and the 1.0 M KFSI in TEG electrolyte (solid lines

ChemPhysChem

Research Article
doi.org/10.1002/cphc.202400606

**Chemistry
Europe**
European Chemical
Societies Publishing

[FSI$_1$-K-TEG$_1$] model, and least in the [FSI$_1$-K-TEG$_2$] model. The absolute shifts, both experimental and computed, cannot be used to explicitly determine the exact speciation, but we suggest, based on the very small shift found for the 0.5–2.0 M electrolytes, that mainly cation-coordinated FSI is present for all, while the nature of the cation-anion species cannot be determined. The peak broadening as a function of salt concentration is most likely both due to more local coordination situations being sampled, as is often the case for more concentrated electrolytes, and, also contributing to the observed shift, a consequence of increased permittivity – as previously shown for the related TFSI anion in several solvents.[15]

The selected TEG region can be divided into four ranges at 836–840 cm^{-1}, 861 cm^{-1}, 892 cm^{-1} (left shoulder) and 908 cm^{-1}. The first peak corresponds to a CH$_3$ bending vibration (δ_{CH3}) with a resultant slight C–O–C bending vibration (δ_{C-O-C}) of the same side chain. With increasing salt concentration, the intensity decreases, and the peak broadens. On the one hand, the decrease in intensity is due to the reduced proportion of TEG in the electrolyte and this vibration only exists for TEG. On the other hand, the artificial peak from the [FSI$_1$-K-TEG$_2$] complex exhibits the highest intensity but the amount of this complex decreases with increasing salt concentration. The increasing width of the experimental peak can be explained by the overlay of several vibrations, while for pure TEG and at 0.5 M concentration, only "free" TEG and sporadically coordinated TEG are present. The peak at 861 cm^{-1} can only be assigned to an impurity in the KFSI salt, as although the intensity of this peak increases with rising salt concentration, no corresponding artificial K-FSI peak is to be found in this region. The left shoulder, labelled with number 2, and the peak, labelled with number 3, are due to δ_{CH3} vibration, which additionally cause a C–O stretching vibration (ν_{C-O}) of the side chain. With increasing salt concentration, the left shoulder at 892 cm^{-1} disappears. Since this shoulder is only visible in the artificial spectra of "free" TEG and [K-TEG$_1$]$^+$, it indicates that predominantly [FSI$_1$-K-TEG$_1$] and [FSI$_1$-K-TEG$_2$] are present from a concentration of 1.0 M and onwards.

Diffusion of KFSI in TEG

In theory, the Nyquist plot for a symmetric metal-metal cell consists of three semicircles and can be explained with the proposed equivalent circuit (Figure 7a).[4-5,16] At high frequencies (> 1.5 kHz), the electric resistance (R$_E$) of the cell with 1.0 M KFSI in TEG is measured (Figure 7b). This includes the ohmic resistances of the cables, Swagelok cell, current collectors, metal potassium electrodes and electrolyte.[17] In the middle range of frequency (1.5 kHz to 0.35 Hz), the first semicircle emerges, which upon closer inspection corresponds to two overlapped semicircles. These two semicircles are particularly noticeable in the Bode plot (Figure 7c). The first region of the semicircle extends from 1.5 kHz to 35 Hz and can be assigned to the impedance of the SEI layer (Z$_{SEI}$) and thus characterized the ion transport through the SEI. Following that is the range from 35 Hz to 0.35 Hz, which can be allocated to the charge transfer impedance (Z$_{ct}$) and describes the charge transfer at the SEI electrolyte interface. Z$_{SEI}$ is attributed to the higher frequencies, as the typical resonance frequency of the SEI is higher as compared to that of the charge transfer process, and during the resting time, the SEI impedance is formed (Figure S2). For fitting the Nyquist plot, resistances R were used for ion migration through the layers and constant phase elements (CPEs) were used for the non-perfectly homogeneous layer of adsorbed ions.[5]

The low frequency range (< 0.5 Hz) responds to the diffusion impedance Z$_D$ and is also known as finite-length Warburg impedance with transmissive boundary or Warburg short (W$_s$).[5,16,18]

The fit deviates more significantly from the measured data at very low frequencies (Figure S3). This could be due to temperature fluctuations despite the use of the climate chamber, which have a significant influence on the long measurement time of 15 min to 3 hours for frequencies lower than 1 mHz.

To calculate the diffusion coefficient of KFSI in the electrolyte, the resonance frequency f$_D$ of the diffusion impedance Z$_D$ is required. This frequency can be determined when the amount of the imaginary resistance is maximally negative and thus the maximum of the diffusion semicircle is reached
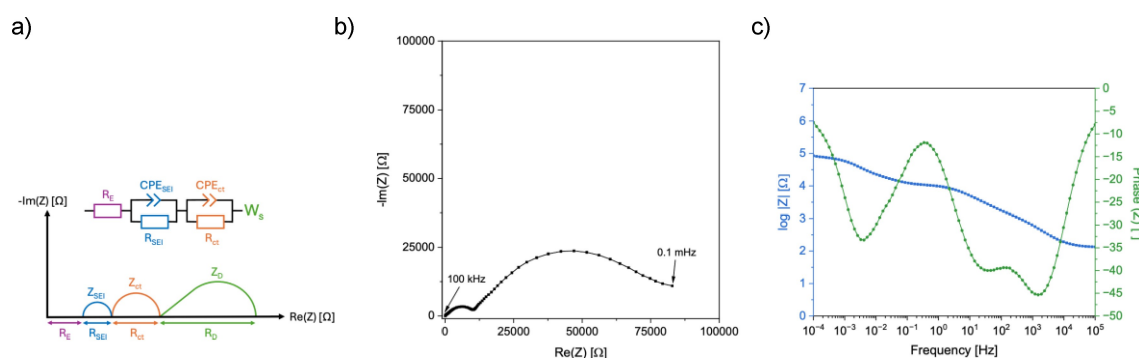

Figure 7. a) General impedance response and proposed equivalent circuit for a symmetric metallic cell, b) Nyquist and c) Bode plot of a symmetric K-metal cell with the 1.0 M KFSI in TEG electrolyte.

ChemPhysChem

Research Article
doi.org/10.1002/cphc.202400606

Chemistry
Europe
European Chemical
Societies Publishing

(Figure S3). Following, the diffusion coefficient of the salt (D_{KFSI}) can be expressed as

where L is the distance between the potassium electrodes.[5] The diffusion coefficient for the cell containing the 1.0 M KFSI in TEG electrolyte was $D = 3.2 \cdot 10^{-9}$ m^{2}s^{-1}. Furthermore, the diffusion coefficients were determined for 0.5 M, 1.5 M and 2.0 M KFSI in TEG (Figure S4). It can be observed that the diffusion coefficient decreases with increasing salt concentration, which is due to increased intermolecular interactions. The diffusion coefficients are comparable to that of DME-based electrolytes and in the upper range of alkali metal electrolytes, much due to the physiochemical properties of potassium.[3a,c,5,19] However, when comparing diffusion coefficients, it must be taken into account that the use of a (different) separator,[20] the cell setup[21] and the temperature can have a significant influence.

Conclusions

In conclusion, TEG is energetically most favourable with z formatted side chains, while FSI is preferred in the *trans* configuration, positioning the fluorine atoms on opposite sides. The coordination of K$^+$ is optimally achieved through tridentate coordination with FSI or through two bridge oxygen atoms of TEG. This study has demonstrated the possibility of coordinating up to SN = 3 and CN = 7 with the complex [FSI$_1$-K-TEG$_2$]. Given that the binding energy for K$^+$ coordination by FSI is higher than that for a K$^+$ coordination by TEG, a KFSI in TEG electrolyte behaves as a WSE. Comparisons between artificial and experimental Raman spectra have shown that at lower KFSI salt concentrations there is a higher presence of "free" TEG and the complex [FSI$_1$-K-TEG$_2$], whereas at higher salt concentrations the complexes [FSI$_1$-K-TEG$_1$] and [K-FSI] are the dominant species. The diffusion coefficient of 1.0 M KFSI in the TEG electrolyte was determined to be $D = 3.2 \cdot 10^{-9}$ m^{2}s^{-1} using impedance spectroscopy. Thus, the coordination of the glyoxal-based potassium electrolyte could be clarified depending on the concentration and due to the good diffusion properties of the electrolyte, this electrolyte can be used well in potassium-based energy storage systems.

Experimental and Computational

Electrolyte Preparation

KFSI (99.9%, *Solvionic*) and TEG (*Weylchem*) were used for the electrolyte preparation. KFSI was used as received, while TEG was dried using an overpressure Schlenk filtration with alkaline Al$_2$O$_3$ (pre-dried at 260 °C) to reach a water content of < 16 ppm (as measured by Karl Fischer titration). The electrolytes, with salt concentrations between 0.5 and 2.0 M KFSI, which corresponds to molar ratios KFSI:TEG from 1:8 to 1:1.5, were prepared by magnetic stirring at 400 rpm for 12 h in an argon filled glovebox with H$_2$O and O$_2$ < 1 ppm.

Computational Chemistry

The geometry optimization of FSI and TEG conformers and subsequently their complexes with K$^+$ ([K-TEG]$^+$, [K-FSI] and [FSI–K–TEG$_{1-2}$]) were carried out as DFT calculations using Gaussian 16 employing the M06-2X functional[22] and the 6-311+G(d,p) basis set,[23] both in vacuum and using a polarisable continuum model (PCM) for TEG ($\varepsilon = 2.55$) as the dielectric medium. The binding energies (ΔE_{BE}) for the complexes were calculated as:

$$\Delta E_{BE} = E_{complex} - E_{\Sigma \, ions/solvent} = E_{complex} - \left(E_{K^+} + x E_{ligands} \right) \quad (2)$$

The artificial Raman spectra, using the 3rd energy derivatives of the converged minimum energy structures data, were constructed using the GaussSum 3.0.2 software with a frequency scaling factor of 0.946,[24] a full width at half maximum (FWHM) of 10 cm^{-1}, an excitation wavelength of 1064 nm, and a temperature of 293.15 K.

Several possible structures were identified in the geometry optimization, but we focus only on the four structures with the lowest energy or those with an energy difference of maximum +20 kJ/mol from the most stable. Furthermore, only the structures and energies of the PCM calculations are discussed, as only minor differences were obtained when compared to the vacuum method and the PCM model is closer to reality.

The ESP map, which enables the visualization of the charge distribution of molecules, was employed to ascertain potential coordination sites of the ligands. To understand the thermodynamic stability of electrolytes, their HOMO and LUMO energy levels were calculated.

Raman Spectroscopy

The Raman spectra were measured with a MultiRam FT-Raman (*Bruker*) spectrometer using a 1064 nm Nd:YAG laser as the excitation source. The data were recorded between 0 and 3500 cm^{-1} with a resolution of 2 cm^{-1} and 2000 scans were sampled.

Electrochemical Impedance Spectroscopy

Symmetric Swagelok cells, having metallic potassium (99%, *Thermo Fisher Scientific*) as electrodes, divided by polyether ether ketone (PEEK) spacer (1 mm thickness) filled with ~500 μL 0.5–2.0 M KFSI in TEG, were assembled inside an argon filled glovebox and then connected to a battery cycler (MPG-2, *Biologic*) and placed in a climate chamber (model ED56, *BINDER*), set to 25 °C. To get a stable final impedance the cells were rested at open circuit potential for 72 h with a data acquisition every 2 h, with a 10 mV amplitude and in a frequency range from 100 kHz to 50 mHz (Figure S2). The final spectra were recorded from 100 kHz to 0.1 mHz. All spectra were fitted using ZView version 4.0.

Conflict of Interests

The authors declare no conflict of interest.

Data Availability Statement

The data that support the findings of this study are available from the corresponding author upon reasonable request.

[1] a) M. Armand, J. M. Tarascon, *Nature* **2008**, *451*, 652–657; b) M. S. Whittingham, *Chem. Rev.* **2004**, *104*, 4271–4302.

[2] a) T. Hosaka, K. Kubota, A. S. Hameed, S. Komaba, *Chem. Rev.* **2020**, *120*, 6358–6466; b) X. Min, J. Xiao, M. Fang, W. Wang, Y. Zhao, Y. Liu, A. M. Abdelkader, K. Xi, R. V. Kumar, Z. Huang, *Energy Environ. Sci.* **2021**, *14*, 2186–2243; c) R. Rajagopalan, Y. Tang, X. Ji, C. Jia, H. Wang, *Adv. Funct. Mater.* **2020**, *30*, 1909486; d) Y.-S. Xu, S.-Y. Duan, Y.-G. Sun, D.-S. Bin, X.-S. Tao, D. Zhang, Y. Liu, A.-M. Cao, L.-J. Wan, *J. Mater. Chem. A* **2019**, *7*, 4334–4352; e) X. Li, J. Li, L. Ma, C. Yu, Z. Ji, L. Pan, W. Mai, *Energy Environ. Mater.* **2022**, *5*, 458–469; f) Y. Lyu, X. Wu, K. Wang, Z. Feng, T. Cheng, Y. Liu, M. Wang, R. Chen, L. Xu, J. Zhou, Y. Lu, B. Guo, *Adv. Energy Mater.* **2021**, *11*, 2000982.

[3] a) S. Dhir, B. Jagger, A. Maguire, M. Pasta, *Nat. Commun.* **2023**, *14*, 3833; b) M. Okoshi, Y. Yamada, S. Komaba, A. Yamada, H. Nakai, *J. Electrochem. Soc.* **2017**, *164*, A54–A60; c) J. Landesfeind, T. Hosaka, M. Graf, K. Kubota, S. Komaba, H. A. Gasteiger, *J. Electrochem. Soc.* **2021**, *168*, 040538; d) R. H. Stokes, *J. Am. Chem. Soc.* **1950**, *72*, 2243–2247.

[4] T. Q. Nguyen, C. Breitkopf, *J. Electrochem. Soc.* **2018**, *165*, E826.

[5] F. Single, B. Horstmann, A. Latz, *J. Phys. Chem. C* **2019**, *123*, 27327–27343.

[6] a) L. Medenbach, L. C. Meyer, A. Balducci, *Electrochem. Commun.* **2021**, *125*, 107001; b) S. Liu, L. C. Meyer, L. Medenbach, A. Balducci, *Energy Storage Materials* **2022**, *47*, 534–541; c) L. H. Heß, A. Balducci, *ChemSusChem* **2018**, *11*, 1919–1926; d) C. Leibing, D. Leistenschneider, C. Neumann, M. Oschatz, A. Turchanin, A. Balducci, *ChemSusChem* **2023**, *16*, e202300161.

[7] a) M. S. Ding, K. Xu, S. Zhang, T. R. Jow, *J. Electrochem. Soc.* **2001**, *148*, A299; b) S. Hess, M. Wohlfahrt-Mehrens, M. Wachtler, *J. Electrochem. Soc.* **2015**, *162*, A3084; c) D. R. Lide, *CRC Handbook of Chemistry and Physics*, 84th Edition, CRC Press LLC, Boca Raton, **2003**.

[8] a) F. Zhang, X. Wang, M. Wu, A. Yang, Y. Li, M. Man, Y. Li, J. Guo, *ACS Energy Lett.* **2023**, *8*, 4895–4902; b) P. N. Le Pham, V. Gabaudan, A. Boulaoued, G. Åvall, F. Salles, P. Johansson, L. Monconduit, L. Stievano, *Energy Storage Mater.* **2022**, *45*, 291–300.

[9] T. A. Pham, K. E. Kweon, A. Samanta, V. Lordi, J. E. Pask, *J. Phys. Chem. C* **2017**, *121*, 21913–21920.

[10] J. B. Goodenough, Y. Kim, *Chem. Mater.* **2010**, *22*, 587–603.

[11] a) Y.-X. Yao, X. Chen, C. Yan, X.-Q. Zhang, W.-L. Cai, J.-Q. Huang, Q. Zhang, *Angew. Chem. Int. Ed.* **2021**, *60*, 4090–4097; b) J. Li, Y. Hu, H. Xie, J. Peng, L. Fan, J. Zhou, B. Lu, *Angew. Chem. Int. Ed.* **2022**, *61*, e202208291; c) Z. Wang, B. Zhang, *Energy Mater. Devices* **2023**, *1*, 9370003.

[12] a) B. Ma, P. Sittisomwong, J. Ma, P. Bai, *ACS Appl. Energy Mater.* **2022**, *5*, 7124–7133; b) A. M. Wagaye, T. Yohannes, G. A. Workneh, *ACS Omega* **2024**, *9*, 14406–14418.

[13] a) X. Chen, H.-R. Li, X. Shen, Q. Zhang, *Angew. Chem. Int. Ed.* **2018**, *57*, 16643–16647; b) L. Fan, S. Chen, R. Ma, J. Wang, L. Wang, Q. Zhang, E. Zhang, Z. Liu, B. Lu, *Small* **2018**, *14*, 1801806; c) L. Li, S. Zhao, Z. Hu, S.-L. Chou, J. Chen, *Chem. Sci.* **2021**, *12*, 2345–2356.

[14] H. Wang, D. Yu, X. Wang, Z. Niu, M. Chen, L. Cheng, W. Zhou, L. Guo, *Angew. Chem. Int. Ed.* **2019**, *58*, 16451–16455.

[15] A. Martinelli, A. Matic, P. Johansson, P. Jacobsson, L. Börjesson, A. Fernicola, S. Panero, B. Scrosati, H. Ohno, *J. Raman. Spectrosc.* **2011**, *42*, 522–528.

[16] F. Wohde, M. Balabajew, B. Roling, *J. Electrochem. Soc.* **2016**, *163*, A714.

[17] W. Choi, H.-C. Shin, J. M. Kim, J.-Y. Choi, W.-S. Yoon, *J. Electrochem. Sci. Technol.* **2020**, *11*, 1–13.

[18] J. R. Macdonald, W. B. Johnson, *Impedance Spectroscopy: Theory, Experiment, and Applications*, 3rd Edition, John Wiley & Sons, Inc., New York, **2018**.

[19] a) M. Saito, T. Fujinami, S. Yamada, T. Ishikawa, H. Otsuka, K. Ito, Y. Kubo, *J. Electrochem. Soc.* **2017**, *164*, A2872; b) J. Fawdon, J. Ihli, F. L. Mantia, M. Pasta, *Nat. Commun.* **2021**, *12*, 4053; c) A. A. Wang, A. B. Gunnarsdóttir, J. Fawdon, M. Pasta, C. P. Grey, C. W. Monroe, *ACS Energy Lett.* **2021**, *6*, 3086–3095; d) J. D. Bazak, J. P. Allen, S. A. Krachkovskiy, G. R. Goward, *J. Electrochem. Soc.* **2020**, *167*, 140518; e) S.-I. Lee, U.-H. Jung, Y.-S. Kim, M.-H. Kim, D.-J. Ahn, H.-S. Chun, *Korean J. Chem. Eng.* **2002**, *19*, 638–644.

[20] S. Drvarič Talian, J. Moškon, R. Dominko, M. Gaberšček, *ACS Appl. Mater. Interfaces* **2017**, *9*, 29760–29770.

[21] S. Drvarič Talian, J. Moškon, E. Tchernychova, R. Dominko, M. Gaberšček, *J. Electrochem. Soc.* **2023**, *170*, 110529.

[22] Y. Zhao, D. G. Truhlar, *Theor. Chem. Account* **2008**, *120*, 215–241.

[23] M. P. Andersson, P. Uvdal, *J. Phys. Chem. A* **2005**, *109*, 2937–2941.

[24] D. O. Kashinski, G. M. Chase, R. G. Nelson, O. E. Di Nallo, A. N. Scales, D. L. VanderLey, E. F. C. Byrd, *J. Phys. Chem. A* **2017**, *121*, 2265–2273.